KTH Industrial Engineering
and Management

ELECTRONIC STRUCTURE STUDIES AND METHOD DEVELOPMENT FOR COMPLEX MATERIALS

ANDREAS ÖSTLIN

Licentiate Thesis
School of Industrial Engineering and Management, Department of Materials Science and Engineering, KTH, Sweden, 2013

Materialvetenskap
KTH
SE-100 44 Stockholm
Sweden

ISRN KTH/MSE–13/02–SE+AMFY/AVH
ISBN 978-91-7501-646-7

Akademisk avhandling som med tillstånd av Kungliga Tekniska Högskolan framläggs till offentlig granskning för avläggande av licentiatexamen torsdagen den 7 Mar. 2013 kl 10:00 i konferensrummet, Materialvetenskap, Kungliga Tekniska Högskolan, Brinellvägen 23, Stockholm.

Tryck: Universitetsservice US AB

Abstract

Over the years electronic structure theory has proven to be a powerful method with which one can probe the behaviour of materials, making it possible to predict properties that are difficult to measure experimentally. The numerical tools needed for these methods are always in need of development, since the desire to calculate more complex materials pushes this field forward. This thesis contains work on both this implementational and developmental aspects.

In the first part we investigate the structural properties of the $6d$ transition metals using the exact muffin-tin orbitals method. It is found that these elements behave similarly to their lighter counterparts, except for a few deviations. In these cases we argue that it is relativistic effects that cause this anomalous behaviour.

In the second part we assess the Padé approximant, which is used in several methods where one wants to include many-body effects into the electronic structure. We point out difficulties that can occur when using this approximant, and propose and evaluate methods for their solution.

Preface

List of included publications:

I **First-principles calculation of the structural stability of 6d transition metals**
A. Östlin and L. Vitos, *Physical Review B* **84**, 113104 (2011).

II **One-particle spectral function and analytic continuation for many-body implementation in the exact muffin-tin orbitals method**
A. Östlin, L. Chioncel, and L. Vitos, *Physical Review B* **86**, 235107 (2012).

Comment on my own contribution

Paper I: All calculations, literature survey, data analysis, writing the manuscript.

Paper II: All calculations, code development, literature survey, data analysis, writing the main part of the manuscript.

Contents

Chapter 1

Introduction

One of the most fascinating aspects of condensed matter physics is that quite complex phenomena can arise from a seemingly simple starting point. Matter is, at a certain energy scale, built up of positively charged ions surrounded by negatively charged electrons. Even though the physics of single ions and electrons on their own are quite well understood, the physics that emerge when one brings together a macroscopic amount of ions and electrons can become very complex. For example, metals and insulators behave quite differently (metals conduct while insulators do not) even though they are built up of the same kind of particles. Also, even more complex phenomena can be found in nature, like magnetism and superconductivity. One of the fields in physics which try to explain these phenomena is *electronic structure theory*, where the goal is to calculate energies and wave functions of the constituent electrons in matter by solving a many-particle Schrödinger equation. Using this information, much of the complex behaviour of matter can be explained.

Since the 1960s, *density functional theory* (DFT) has been one of the cornerstones of electronic structure theory [1, 2, 3]. Using many kinds of different implementations, DFT has been able to describe several properties of real materials. One of the main merits of DFT is that one is able to calculate properties of materials that are difficult, or even impossible, to probe by experimental techniques. The first part of this thesis investigates a situation where this is the case, namely the $6d$-series of the transition metals, which have not been found in nature. Even though these elements (nr. 103-111 in the periodic table) have all been synthesized, no macroscopic sample has ever been produced. Hence, investigation of their electronic structure has been out of reach for experiment. There are however classes of materials where DFT has been found wanting. One such class are systems where *strong correlations* are important. Here the physics is mainly governed by the interaction between electrons, an effect that is only handled approximately in DFT.

Parallel with DFT, *many-body methods* have shown great success in advancing our understanding of condensed matter. These methods have in common that they start with a so-called *model Hamiltonian*, which is an approximation of the full electronic Hamil-

tonian. In these Hamiltonians, only terms which are believed to be important for the physical effects of interest are kept. The properties of interest are then computed from these simplified models using analytical and numerical methods. Using this approach, advances have been made in many difficult problems. One prominent example is in the field of strongly correlated systems. However, these many-body methods have the drawback that they have difficulties in producing quantitative data for real materials.

Since both DFT and many-body techniques seem to complement each other, one being strong where the other is weak and vice versa, finding a way to merge these methods would be promising. Recently one of the available many-body techniques, namely *dynamical mean field theory* (DMFT), together with DFT in the local density approximation (LDA), has shown great promise in describing real systems with strong correlations [4, 5]. These so-called LDA+DMFT methods have only existed for a few decades, and no clear picture of optimal implementation has yet emerged. Since density functional and many-body methods have evolved independently over the years, their merging is by no means trivial. One issue which has surfaced in some of these methods is the need for *analytic continuation* in the complex plane. This is because important functions are calculated in one part of the complex plane, while they are needed in another part. Hence precise extrapolation of these functions are needed. The second part of this thesis scrutinizes this issue.

1.1 Overview

The key ideas behind first-principles methods are given in chapter 2. Density functional theory is introduced in section 2.1 and its implementation in the exact muffin-tin orbitals method is outlined in section 2.2. In the latter section the many-body implementation for the exact muffin-tin orbitals method and the need for analytic continuation is also discussed. This gives the motivation to the work in Paper II.

Chapter 3 discusses the theory of transition metals, which is related to Paper I. We discuss the general behaviour and trends of the transition metal series, and connect these with the transactinide transition metals.

In chapter 4 the numerical methods involved in the analytic continuation is outlined and discussed. New methods are then proposed and evaluated.

A summary with concluding remarks is found in chapter 5.

Chapter 2

First principles theory

The goal of electronic structure theory is to solve the N-particle Schrödinger equation

$$H\Psi = E\Psi, \tag{2.1}$$

where $\Psi = \Psi(\mathbf{r}_1, ..., \mathbf{r}_N, \mathbf{R}_1, ..., \mathbf{R}_M)$ is the N-particle wave function for N electrons with positions $\mathbf{r}_i$ and M ions with positions $\mathbf{R}_i$. Ψ is an eigenfunction of the electronic Hamiltonian H

$$\begin{aligned} H = &- \frac{\hbar^2}{2m_e}\sum_{i=1}^{N}\nabla_{\mathbf{r}_i}^2 - \frac{\hbar^2}{2}\sum_{i=1}^{M}\frac{\nabla_{\mathbf{R}_i}^2}{M_i} - e^2\sum_{i=1}^{N}\sum_{j=1}^{M}\frac{Z_j}{|\mathbf{r}_i - \mathbf{R}_j|} \\ &+ \frac{e^2}{2}\sum_{i\neq j}^{N}\frac{1}{|\mathbf{r}_i - \mathbf{r}_j|} + \frac{e^2}{2}\sum_{i\neq j}^{M}\frac{Z_i Z_j}{|\mathbf{R}_i - \mathbf{R}_j|}, \end{aligned} \tag{2.2}$$

consisting of electrons with mass m_e and ions with mass M_i. The first two terms account for the kinetic energy of the electrons and the ions, respectively. The third term represents the Coulomb interaction between the electrons and the ions, while the last two terms corresponds to the electron-electron and ion-ion interaction, respectively.

For more than a few electrons and ions the solution of Eq. (2.1) becomes intractable and approximations are usually made. One such approximation is the *Born-Oppenheimer approximation*, which makes use of the fact that the weight of an ion is larger than the electron mass by several orders of magnitude ($M_i \gtrsim 1000m_e$). This implies that the electrons move faster than the ions and that they can quickly readjust if the ion configuration changes. The kinetic energy term from the ions drops out and the ions are viewed as a static background.

Hence Eq. (2.1) is reduced to

$$\begin{aligned} &\left(-\frac{\hbar^2}{2m_e}\sum_{i=1}^{N}\nabla_{\mathbf{r}_i}^2 - e^2\sum_{i=1}^{N}\sum_{j=1}^{M}\frac{Z_j}{|\mathbf{r}_i - \mathbf{R}_j|} + e^2\sum_{i\neq j}^{N}\frac{1}{|\mathbf{r}_i - \mathbf{r}_j|}\right)\Psi \\ &= (T + V_{ext} + V)\Psi = E\Psi, \end{aligned} \tag{2.3}$$

where T is the kinetic energy, V_{ext} is the external potential from the static background and V is the electron-electron (Hartree) interaction. From now on, we will use atomic Rydberg units ($\hbar = 2m_e = e^2/2 = 1$) throughout the thesis. Notice that in Eq. (2.3), T and V are *universal*, i.e. they are the same for all interacting N-electron systems. It is V_{ext} that makes the Hamiltonian unique. Hence, giving the ionic charges Z_i and positions $\mathbf{R}_i$ as input, one should in principle be able to solve Eq. (2.3) for any system without further approximations. This is the main idea of so-called *first principles* (or *ab initio*) methods. However, more approximations can, and must often, be made. One of the most popular ways to solve Eq. (2.3) in an approximate fashion is by using density functional theory, which is introduced in the next section.

2.1 Density functional theory

Since its introduction in the 1960s, density functional theory has become one of the most powerful methods in electronic structure theory. There exist several ways to derive the DFT formalism, and we closely follow the treatment given in Ref. [6]. The foundation of DFT rests on the seminal work of Hohenberg and Kohn [1]. In that work the *Hohenberg-Kohn theorem* is introduced and proved, which states that the expectation value $O = \langle\Psi|\mathcal{O}|\Psi\rangle$ of any operator $\mathcal{O}$ is a *unique* functional of the ground-state density $n(\mathbf{r})$, $O = O[n(\mathbf{r})]$. Hence, if we know the ground-state density of a certain N-particle system, we could calculate any physical observable without having to calculate the many-body wave functions. This theorem implies that no two Hamiltonians and hence no two external potentials (since the external potential uniquely defines the Hamiltonian) can give the same ground-state density of a system. It should also be mentioned that the Hohenberg-Kohn theorem can be extended to include spin-polarized densities, as well as degenerate ground-states.

One implication of the Hohenberg-Kohn theorem is that the ground-state energy of a system can be written as functional, since it is the expectation value of the Hamiltonian:

$$E[n] = \langle\Psi[n]|T + V_{ext} + V|\Psi[n]\rangle\,. \tag{2.4}$$

This will be of use later on.

Even though the Hohenberg-Kohn theorem is powerful, it does not give a computational method to find the ground-state density. This is however given by the Kohn-Sham formalism [2]. The main idea of this formalism is to use a noninteracting system that has an external (effective) potential V_{eff} which gives the same ground-state density as for the interacting system with potential V_{ext}. If the effective Hamiltonian of the noninteracting system is given by

$$H_{eff} = T_{eff} + V_{eff}, \tag{2.5}$$

then its energy functional becomes

$$E_{eff}[n] = T_{eff}[n] + \int d\mathbf{r} V_{eff}(\mathbf{r}) n(\mathbf{r}). \tag{2.6}$$

Since the effective system is noninteracting, we can in this case obtain the ground-state density by first solving the Schrödinger-like single-particle *Kohn-Sham equations*

$$\left(-\nabla^2_{\mathbf{r}_i} + V_{eff}\right)\Psi_i = E_i \Psi_i, \tag{2.7}$$

where the Ψ_i are the single-electron orbitals, and then perform the sum

$$n_{eff}(\mathbf{r}) = \sum_{i=1}^{N} |\Psi_i(\mathbf{r})|^2. \tag{2.8}$$

The orbitals Ψ_i will correspond to the N lowest eigenvalues E_i, by virtue of the Pauli exclusion principle.

Now, by construction we want that the noninteracting density should equal the interacting density, $n(\mathbf{r}) = n_{eff}(\mathbf{r})$. Rewriting the interacting energy functional in Eq. (2.4) in the following way,

$$\begin{aligned} E[n] =& T_{eff}[n] + \left(T[n] - T_{eff} + V[n] - \frac{1}{2}\int d\mathbf{r} \int d\mathbf{r}' \frac{n(\mathbf{r})n(\mathbf{r}')}{|\mathbf{r}-\mathbf{r}'|} \right) \\ &+ \frac{1}{2}\int d\mathbf{r} \int d\mathbf{r}' \frac{n(\mathbf{r})n(\mathbf{r}')}{|\mathbf{r}-\mathbf{r}'|} + \int d\mathbf{r} V_{ext}(\mathbf{r}) n(\mathbf{r}) \\ :=& T_{eff}[n] + \frac{1}{2}\int d\mathbf{r} \int d\mathbf{r}' \frac{n(\mathbf{r})n(\mathbf{r}')}{|\mathbf{r}-\mathbf{r}'|} + \int d\mathbf{r} V_{ext}(\mathbf{r}) n(\mathbf{r}) + E_{xc}[n], \end{aligned} \tag{2.9}$$

will prove convenient. All information about the electron interactions (except for the Hartree term) has been moved to the *exchange-correlation energy* functional $E_{xc}[n]$. According to the Hohenberg-Kohn theorem, the ground-state density should minimize the energy functional in Eq. (2.9). Hence, by taking the variation with respect to $n(\mathbf{r})$ we get that

$$\frac{\delta E[n]}{\delta n(\mathbf{r})} = \frac{\delta T_{eff}[n]}{\delta n(\mathbf{r})} + \int d\mathbf{r}' \frac{n(\mathbf{r}')}{|\mathbf{r}-\mathbf{r}'|} + V_{ext}(\mathbf{r}) + V_{xc}[n(\mathbf{r})] = 0, \tag{2.10}$$

where $V_{xc}[n(\mathbf{r})] := \frac{\delta E_{xc}[n]}{\delta n(\mathbf{r})}$. The same should hold for the noninteracting system, i.e.,

$$\frac{\delta T_{eff}[n]}{\delta n(\mathbf{r})} + V_{eff}(\mathbf{r}) = 0. \tag{2.11}$$

Inserting Eq. (2.11) in Eq. (2.10), we finally get that

$$V_{eff}(\mathbf{r}) = V_{ext}(\mathbf{r}) + \int d\mathbf{r}' \frac{n(\mathbf{r}')}{|\mathbf{r}-\mathbf{r}'|} + V_{xc}(\mathbf{r}). \tag{2.12}$$

The scheme is now as follows: First a guess is made for a starting density $n(\mathbf{r})$ which is used as input in Eq. (2.12). The potential $V_{eff}(\mathbf{r})$ is then used to solve the Kohn-Sham equations (Eq. (2.7)). The single-particle orbitals Ψ_i thus obtained are used to construct a new density from Eq. (2.8). This density is then used as input in Eq. (2.12) to get a new potential, and this cycle is repeated until self-consistency is reached. The final density will then not only be the correct ground-state density for the noninteracting system, but also for the interacting system by construction.

This procedure is formally exact. However, no explicit form for the exchange-correlation potential V_{xc} is known, and one has to resort to using approximations for this quantity. One of the most common approximations is the *local density approximation* (LDA), where the exchange-correlation functional E_{xc} is assumed local,

$$E_{xc}[n] = \int d\mathbf{r} \epsilon_{xc}[n] n(\mathbf{r}). \tag{2.13}$$

Here the exchange-correlation energy per electron ϵ_{xc} is that for a uniform electron gas, which can be parametrized in various ways. The parametrization used in this thesis is due to Perdew and Wang [7]. For other approximations to the exchange-correlation potential the reader is referred to the literature [3, 6].

2.2 Exact muffin-tin orbitals method

At the present time there exist many different formalisms which enables the solution of the Kohn-Sham equations (2.7). One popular family of methods are the $muffin-tin$ methods. The idea behind these methods is to approximate the effective potential V_{eff} by dividing space into two parts. The first part consists of spheres of a fixed radius s_R centered around the lattice sites $\mathbf{R}_i$. Inside these spheres the potential is assumed to be spherically symmetric. The second part is the space outside the spheres, called the *interstitial*, where the potential is assumed to be a constant V_0. These conditions can be expressed as

$$V_{eff}(\mathbf{r}) \approx V_{mt}(\mathbf{r}) := V_0 + \sum_R (V_R(r_R)) - V_0), \tag{2.14}$$

where we introduce $\mathbf{r}_R := r_R \hat{r}_R = \mathbf{r} - \mathbf{R}$ and omit the vector notation for R. $V_R(r_R)$ equals V_0 for $r_R \geqslant s_R$ by definition. The Kohn-Sham equations are solved in each region separately. Inside the spheres, Eq. (2.7) simplifies to a radial Schrödinger equation and in the interstitial to a Helmholtz equation. After solving these equations using certain expanded basis functions, the problem of solving the differential equation (2.7) is reduced to the algebraic problem of matching the expansion coefficients.

In the following we present this scheme for the exact muffin-tin orbitals (EMTO) method [8, 9, 10, 11, 12]. This method allows the muffin-tin spheres to overlap, which has been shown to produce a better approximation to the full potential [8, 13, 14]. In the EMTO

method the Kohn-Sham orbitals Ψ_i are expanded in *exact muffin-tin orbitals* $\bar{\psi}^a_{RL}$, viz.

$$\Psi_i(\mathbf{r}) = \sum_{RL} \bar{\psi}^a_{RL}(E_i, \mathbf{r}_R) v^a_{RL,i}, \tag{2.15}$$

where $v^a_{RL,i}$ are the expansion coefficients, chosen such that Eq. (2.15) solves the Kohn-Sham equations in all space. We use the formalism that $L := (\ell, m)$, where ℓ and m are the orbital and magnetic quantum numbers, respectively. For the interstitial region we use *screened spherical waves* ψ^a_{RL} as basis functions, which solves the Helmholtz equation

$$\left(\nabla^2 + \kappa^2\right) \psi^a_{RL}(\kappa^2, \mathbf{r}_R) = 0, \tag{2.16}$$

where $\kappa^2 := E - V_0$, and E is the energy. The boundary conditions for this equation are given in combination with non-overlapping spheres with radius a_R centered around R. Inside the spheres the basis functions are chosen to be *partial waves*, which are products of the solutions to the radial Schrödinger equation,

$$\frac{\partial^2(r_R \phi_{R\ell}(E, r_R))}{\partial r^2} = \left(\frac{\ell(\ell+1)}{r_R^2} + V_R(r_R) - E \right) r_R \phi_{R\ell}(E, r_R), \tag{2.17}$$

and real spherical harmonics, viz.

$$\phi^a_{RL}(E, \mathbf{r}_R) \sim \phi_{R\ell}(E, r_R) Y_L(\hat{r}_R). \tag{2.18}$$

They are defined for general complex energies and for $r_R \geqslant s_R$. The matching condition should now be set up between $\phi^a_{RL}(E, \mathbf{r}_R)$ and $\psi^a_{RL}(\kappa^2, \mathbf{r}_R)$ at a_R. However, since we want the possibility of overlapping potential spheres, usually $s_R > a_R$. Hence a free-electron solution $\varphi^a_{R\ell}(E, \mathbf{r}_R)$ is introduced, which joins continuously and differentable to the partial waves at s_R and continuously to the screened spherical wave at a_R.
Matching of all coefficients will lead to the *kink cancellation equation*,

$$\sum_{RL} a_R \left(S^a_{RLR'L'}(\kappa_i^2) - \delta_{RR'}\delta_{LL'} D^a_{RL}(E_i) \right) v^a_{RL,i} = 0, \tag{2.19}$$

where D^a_{RL} denotes the EMTO logarithmic derivative function [11, 12], and $S^a_{RLR'L'}$ is the slope matrix [10]. This defines the *kink matrix* for a general complex energy z, viz.

$$K^a_{RLR'L'}(z) := \delta_{RR'}\delta_{LL'} D^a_{RL}(z) - S^a_{RLR'L'}(z). \tag{2.20}$$

A solution of Eq. (2.19) will give the single-electron eigenvalues E_i and wave functions Ψ_i. The EMTO method solves Eq. (2.19) by the Green's function method, which uses the path operator $g^a_{R'L'RL}$, defined as the inverse of the kink matrix (2.20),

$$\sum_{R''L''} K^a_{R'L'}(z) g^a_{R''L''RL}(z) := \delta_{RR'}\delta_{LL'}. \tag{2.21}$$

The eigenvalues will be the poles of $g^a_{R'L'RL}(z)$. This is a Green's function, since it is the inverse (neglecting normalization) of the operator $(z - H_{eff})$, hence the name "Green's

function method". If we have translational symmetry, the sum over site index in Eqs. (2.19) and (2.21) is over the atoms in the primitive cell. The kink matrix, path operator and slope matrix will then depend on the Bloch **k**-vector in the first Brillouin zone (BZ).

Since the energy derivative of the kink matrix, $\dot{K}^a_{RLR'L'}(z)$, gives the overlap matrix for the EMTO basis set [10], the matrix elements of the properly normalized Green's function become [11, 12]

$$G_{RLR'L'}(z) \;=\; \sum_{R''L''} g^a_{RLR''L''}(z)\dot{K}^a_{R''L''R'L'}(z) - \delta_{RR'}\delta_{LL'}I^a_{RL}(z), \tag{2.22}$$

where $I^a_{RL}(z)$ accounts for the unphysical poles of $\dot{K}^a_{RLR'L'}(z)$. The total number of states at the Fermi level E_F is obtained by using the Cauchy residue theorem, viz.

$$N(E_F) = \frac{1}{2\pi i}\sum_{RLR'L'}\oint G_{RLR'L'}(z)\,dz, \tag{2.23}$$

where the energy integral is carried out along a complex contour that cuts the real axis below the bottom of the valence band and at E_F. The charge density is computed on the same complex contour [8]. We also mention that the above formalism can be generalized to include spin. The reader is referred to Refs. [8, 9] for a more in-depth derivation and description of the EMTO method.

2.2.1 Adding many-body effects

In the EMTO+DMFT method [15], the many-body effects are added to the DFT-level Green's function through a local self-energy $\Sigma_{RLRL'}(z)$ via the Dyson equation

$$[G_{RLR'L'}(\mathbf{k},z)]^{-1} = \left[G^{LDA}_{RLR'L'}(\mathbf{k},z)\right]^{-1} - \delta_{RR'}\Sigma_{RLRL'}(z), \tag{2.24}$$

where $G_{RLR'L'}(\mathbf{k},z)$ is now the *LDA+DMFT* Green's function matrix (suppressing spin indices), computed on the complex contour. The $\mathbf{k}-$integrated LDA+DMFT Green's function, $G_{RLR'L'}(z) = \int_{BZ} G_{RLR'L'}(\mathbf{k},z)d\mathbf{k}$, is analytically continued by the Padé method [15], $G(z) \xrightarrow{\text{Padé}} G(i\omega)$ to the Matsubara frequencies $\omega_j = (2j+1)\pi T$, where $j = 0, \pm 1, ...$, and T is the temperature. From this latter Green's function the *bath* Green's function is computed according to

$$[\mathcal{G}_{RLR'L'}(i\omega)]^{-1} = [G_{RLR'L'}(i\omega)]^{-1} + \delta_{RR'}\Sigma_{RLRL'}(i\omega). \tag{2.25}$$

The many-body problem is solved on the Matsubara axis using a spin-polarized T-matrix fluctuation-exchange (SPTFLEX) solver [16], and the resulting self-energy is then analytically continued to the complex contour $\Sigma(i\omega) \xrightarrow{\text{Padé}} \Sigma(z)$. In Figure 2.1 we illustrate the contours used in the EMTO+DMFT calculations. See section 4.1 for details concerning the Padé approximant.

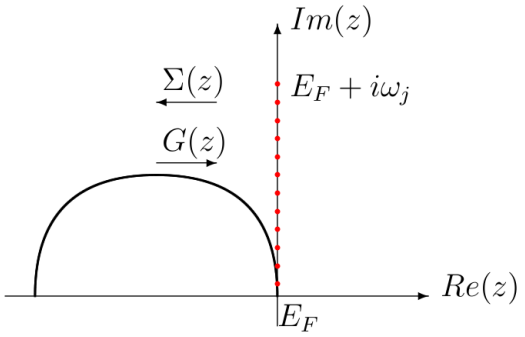

Figure 2.1. Schematic picture of the contours and the analytic continuation used in the EMTO+DMFT method. The Matsubara frequencies are denoted by dots along the imaginary axis relative to the Fermi level E_F. The **k**-integrated Green's function $G(z)$ is calculated for points on the complex contour, here a semi-circle. These are used as input for the analytic continuation to the Matsubara frequencies, on which the many-body problem is solved. The resulting self-energy $\Sigma(i\omega)$ then has to be analytically continued to the points on the semi-circle.

2.3 Relativistic effects

Beginning from Eq. (2.1), the non-relativistic (NR) Schrödinger equation was taken as a starting point for the electronic structure calculations. If relativistic effects are to be taken into account, then one should instead start from the 4-vector Dirac equation [17], describing both electrons and positrons. This is usually denoted as a *fully relativistic* (FR) treatment of the electronic structure problem, and has been implemented into the EMTO method [18]. However, relativistic effects can also be implemented in a perturbative manner using a *Foldy-Wouthuysen transformation* [6, 17] to decompose the 4-vector wave function into a two-component wave function for the electron. If we reintroduce the original units, and use that the momentum can be written as $\mathbf{p} = i\hbar\nabla$, then the new Hamiltonian becomes

$$H = \frac{\mathbf{p}^2}{2m_e} + V(\mathbf{r}) - \frac{\mathbf{p}^4}{8m_e^3c^2} + \frac{\hbar^2}{8m_e^2c^2}\nabla^2 V(\mathbf{r}) + \frac{\mathbf{s}\cdot(\nabla V(\mathbf{r})\times\mathbf{p})}{2m_e^2c^2}, \tag{2.26}$$

where $\mathbf{s} = \sigma/2$ is the spin of the electron. The first two terms constitute the nonrelativistic Hamiltonian used before. The third term is the relativistic mass increase of the electron. The fourth term is the Darwin term and is a correction to the Hamiltonian from the finite extension of the electron, due to quantum fluctuations. The last term is the spin-orbit interaction, which is due to the interaction of the electron spin with the magnetic field stemming from its own orbital motion. The mass enhancement and Darwin terms are collectively called the *scalar relativistic* (SR) terms, since they are scalar quantities. The spin-orbit term on the other hand couples to the spin, and is hence a vector quantity. Keeping only the SR terms in the electronic structure calculations will

be referred to as using the scalar relativistic approximation.

Relativistic terms can become important when heavy elements are involved. This is because the electrons can reach high velocities close to a heavy nucleus, enhancing relativistic effects. In section 3.3 relativistic effects will be further discussed when we investigate the heavy $6d$ transition metals.

Chapter 3

Transition metals

Transition metals are those elements in the periodic table which have incompletely filled d-shells. The first element of this kind is scandium and the last naturally occurring element is gold. Sometimes also the group 12 elements zinc, cadmium and mercury are included in this definition. There are many industrial important elements among the transition metals. One example is iron, which alloyed together with carbon and other transition metals forms various kinds of steels. The $3d$ series also contains metals where electron correlations play an important role, and give rise to magnetic behaviour. As one moves along the different d-series in the periodic table various common trends can be observed. A discussion of these trends is the subject of this chapter.

3.1 Volume and bulk modulus

The physics of the transition metals in the $n+1$ period of the periodic table are mainly governed by the $(n+1)s$- and nd-electrons, where $n \geqslant 3$. For example, in the $3d$-series the $4s$ and $3d$ electrons possess roughly the same energy. The d-electrons are in general more localised than the s-electrons, but they still form bands and participate in the bonding between atoms. This can be seen by studying the density of states of these metals, which in general consists of narrow d-states superimposed over broader s- and p-states [19].

Let us first consider the volume trends seen in the different d-series. We use the *Wigner-Seitz radius* r_{WS}, which is defined as

$$\frac{4\pi r_{WS}^3}{3} := \Omega_{cell}, \tag{3.1}$$

where Ω_{cell} is the volume of the unit cell per atom. The experimental Wigner-Seitz radii of the transition metals can be seen in Figure 3.1. For the $4d$ and $5d$ metals the radii show a parabolic trend, with the bottom of the parabola at the group 8 elements (Ru, Os). For

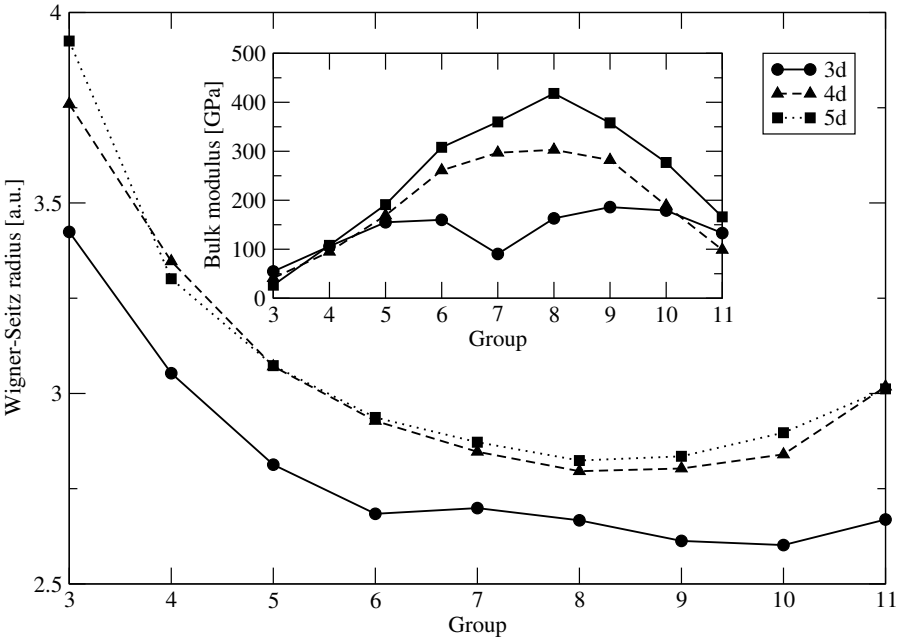

Figure 3.1. The experimentally determined Wigner-Seitz radii in Bohr atomic units and bulk modulus in GPa of the elements in the $3d$, $4d$ and $5d$ series. Data taken from Refs. [8, 20, 21].

the $3d$ metals the parabolic trend shows up twice. The bulk modulus $B = V\frac{\partial^2 E}{\partial V^2}$ is seen plotted in the inset of Figure 3.1. Here, the trend is inverse parabolic.

To explain these trends, consider the atomic orbital radius. The radius for the nd-orbital r_d will be smaller than the radius r_s of the $(n+1)s$-orbital by a factor of $\sim n^2/(n+1)^2$ [19]. Hence it is the radius of the s-states that determine the radius of the atom, and also the volume of the solid. However, the interplay with the d-electrons will determine the effective potential felt by the s-electrons. To see this, notice that the $(n+1)s$ energy level is lower than the nd energy level at the left part of the series, where d-electron occupation is low. This can be seen by the fact that the s-states are doubly occupied (For example, observe the atomic configuration of the group 3 elements Sc: [Ar]$3d^1 4s^2$ and Y: [Kr]$4d^1 5s^2$). This leads to ineffective screening by the d-electrons, and hence the s-electrons feel an increased effective nuclear charge, shrinking their spatial extent. For the group 8 elements the d-electron screening become better, and r_s increases as one goes to the end of the series.

To calculate the volume and bulk modulus using electronic structure theory, the total energy can be calculated for a range of volumes. An equation of state can then be fitted to these values. The equilibrium volume is the volume which minimizes this approximated equation of state, while the equilibrium total energy is the energy corresponding to this volume. In the case of the hcp structure, one more degree of freedom except volume is available, namely the c/a-ratio. This quantity is found by two-dimensional

energy minimization by scanning both a range of volumes and a range of c/a-ratios.

3.2 Crystal structure

Trends can also be found in the crystal structures of the transition metals. Three different structures occur at ambient conditions: body-centered cubic (bcc), face-centered cubic (fcc) and hexagonally closed-packed (hcp). For the $4d$ and $5d$ metals the group 3-4 metals crystallize in hcp, group 5-6 in bcc, group 7-8 in hcp and finally group 9-11 in fcc. The $3d$ elements show some discrepancies, Mn has a complex cubic structure (instead of hcp), Fe is bcc (instead of hcp) and Co is hcp (instead of fcc).

Explanations for this trend was sought from about the 1960s using both empirical and quantitative methods, for references to these early attempts see Refs. [22, 23]. By the 1970s it was found out that the trend can be explained using a very small set of parameters, which is quite remarkable considering the many degrees of freedom in these metals. The theory behind these explanations is the so-called *canonical band theory* [23], which assumes that the energy bands are unhybridized (i.e. no electron transfer between different ℓ-states) and depend only on the crystal structure. This allows the explanation of the hcp-bcc-hcp-fcc trend by considering the d-electron occupation and the shape of the density of states for each lattice for each group of elements. This provides the correct trend for the beginning of the series, but fails to predict the fcc stability for high d-occupation. If hybridization is taken into account, the whole structural trend is captured correctly [24].

To determine the crystal structure from electronic structure theory, one can calculate the equations of state for each lattice type. The structure that has the lowest equilibrium total energy will then be the most stable structure. In this thesis we let the fcc structure be the reference structure, and introduce the quantity $E_{diff} := E_{bcc} - E_{fcc}$. If this quantity is negative, then the bcc structure is favoured over the fcc structure. Otherwise, fcc is favoured. The same quantity can be defined for the hcp-fcc energy difference.

Notice that the hcp-fcc difference will in general be smaller then the bcc-fcc difference. This is because the fcc and hcp lattices have the same number of nearest neighbours (they differ only in next-nearest neighbours), which makes fcc structurally closer to hcp than to bcc.

3.2.1 A classical estimation

If only classical electrostatics would play a role in the structural stabilty of matter, then a bcc lattice would be the most stable configuration in 3D. To see this one can use an argument given by A. W. Overhauser [25]:
Analyze the classical electrostatic energy U of a lattice of N point sources in a box of

length L:

$$U = \frac{1}{2}\sum_{i\neq j}\frac{1}{|\mathbf{R}_i - \mathbf{R}_j|} - \sum_i \int d\mathbf{r}\frac{n}{|\mathbf{r}-\mathbf{R}_i|} + \frac{1}{2}\int\int d\mathbf{r}d\mathbf{r}'\frac{n^2}{|\mathbf{r}-\mathbf{r}'|}. \tag{3.2}$$

Here $\mathbf{R}_i$ are the lattice vectors and $n = N/L^3$ is the constant charge density of the uniform background. The first term is due to the interaction between point sources, the second term is the interaction of the sources with the background and the third term is the interaction of the background with itself. If the $\mathbf{R}_i$'s are the sites of a simple Bravais lattice, then the charge density can be expressed as

$$n(\mathbf{r}) = \sum_i \delta(\mathbf{r}-\mathbf{R}_i) = n\sum_i e^{i\mathbf{G}_i\cdot\,\mathbf{r}}, \tag{3.3}$$

where the $\mathbf{G}_i$'s are the reciprocal lattice vectors. It can be shown (see appendix A) that the electrostatic energy per particle is

$$\frac{U}{N} = \frac{n}{2}\sum_{\mathbf{G}\neq 0}\frac{4\pi}{G^2} - \frac{1}{2L^3}\sum_{\mathbf{q}\neq\mathbf{0}}\frac{4\pi}{q^2}. \tag{3.4}$$

Note that only the first term contains information about the specific lattice structure. Hence, for a given volume of the primitive unit cell, the crystal with the largest magnitude of its first reciprocal vector should be the most stable. Comparing the magnitude of the first reciprocal vector of the bcc lattice $G_{1,bcc} \approx 2.24n^{1/3}\pi$ with that of the fcc lattice $G_{1,fcc} \approx 2.18n^{1/3}\pi$, one can conclude that the bcc lattice should be more stable than the fcc lattice. This estimate will be of use later on. This problem can actually be solved exactly, giving bcc as the most stable lattice. See Ref. [25] for details.

3.3 The $6d$ metals

During the recent decades, more and more of the transactinide elements have been synthesized, the most recent at the time of writing being the element 117 [26]. All of the transactinide transition elements have been synthesized, although only a few number of atoms at a time. These elements are quite unstable, most of the isotopes having half-lives less then seconds, see table 3.1. Since no macroscopic sample of any of these elements has ever been produced, no experimental study of the solid state of them exists. However, there do exist electronic structure theory studies of the transactinides [28, 29, 30, 31], confirming that they in general have similar properties to their lighter counterparts (or *homologues*) in the periodic table, with some exceptions.

In figure 3.2 the calculated Wigner-Seitz radius and bulk modulus is plotted for the $6d$ metals (solid curve), together with the $4d$ metals (dashed curve). The computations are done with the EMTO method, using the scalar relativistic approximation (see section 2.3) and the local density approximation [7]. We also mention that a similar study

Table 3.1. The $6d$ transition metals. Shown are the atomic number, chemical symbol, half-life of the most stable isotope, and name. The half-lives are taken from Ref. [27].

103 Lr, 3.6 h, Lawrencium	**104** Rf, 75.5 s, Rutherfordium	**105** Db, 16 h, Dubnium
106 Sg, 21 s, Seaborgium	**107** Bh, 17 s, Bohrium	**108** Hs, 14 s, Hassium
109 Mt, 0.72 s, Meitnerium	**110** Ds, 7.6 s, Darmstadtium	**111** Rg, 3.6 s, Roentgenium

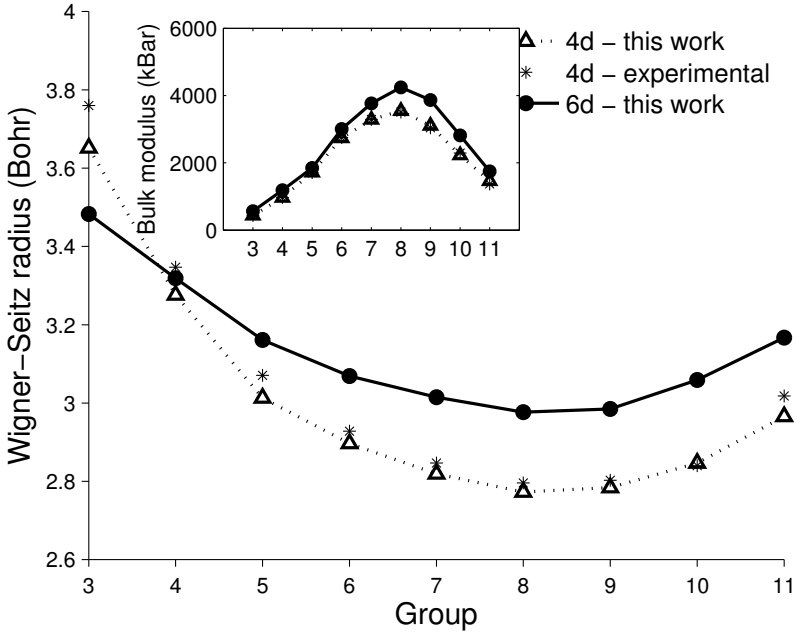

Figure 3.2. Wigner-Seitz radii in Bohr atomic units and bulk modulus in units of kBar for the $4d$ (dashed curve) and $6d$ (solid curve) metals.

was performed independently by Gyanchandani and Sikka [31], using a full-potential method and the generalized gradient approximation. As seen, the same parabolic trend can be seen as for the $4d$ and $5d$ metals, with the smallest volume (and largest bulk modulus) being given by the group 8 element hassium (Hs).

The c/a-ratios are tabulated in table 3.2, and are in good agreement with data taken from Ref. [31]. It is noted that the elements Db, Sg, Ds and Rg all have large c/a-ratios, compared with the ideal ratio $c/a \approx 1.633$. However, as will be seen later, none of these elements crystallize in the hcp structure. That the c/a-ratios can reach values far from

Table 3.2. The calculated hcp c/a-ratios for the $6d$ transition metals. Comparison is made with the full potential results of Ref. [31] where data is available.

	Lr	Rf	Db	Sg	Bh	Hs	Mt	Ds	Rg
This work:	1.58	1.61	1.71	1.74	1.62	1.59	1.64	1.73	1.72
Ref. [31]:	1.55	1.58			1.61	1.58			

the ideal in metals which do not crystallize in the hcp structure was also found by Shang et al. [32] using a projector-augmented wave method.

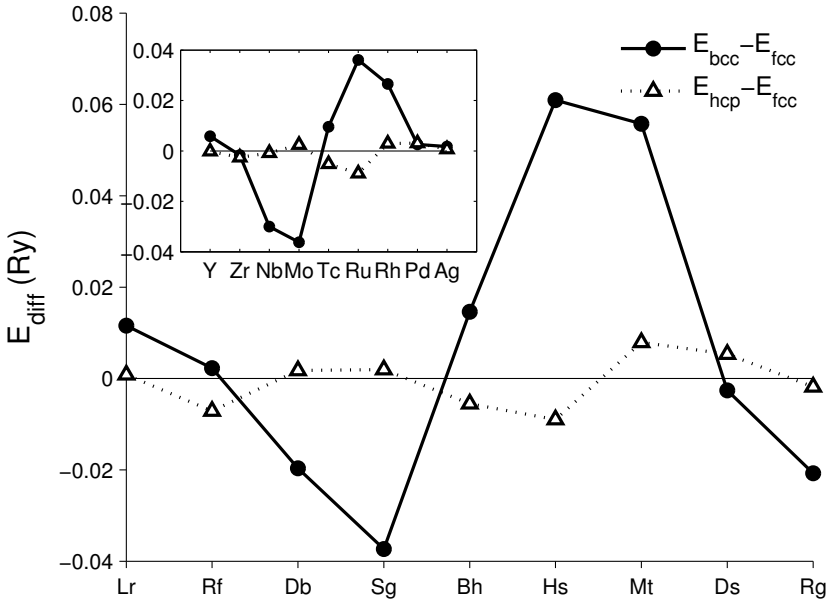

Figure 3.3. Structural energy differences for the $6d$ metals. Inset: Structural energy differences for the $4d$ metals. The scalar relativistic approximation was used for both series.

In figure 3.3 the energy differences between the different crystal structures is seen for the $4d$ and $6d$ metals. For the $4d$ metals the correct hcp-bcc-hcp-fcc trend is captured, and good agreement is found with the data given in Ref. [23]. For the $6d$ metals the topologies of the energy difference curves are similar to the ones given for the lighter transition metals, with the marked exception of the last two metals darmstadtium (Ds) and roentgenium (Rg), which are predicted to crystallize in the bcc structure instead of the fcc structure. Especially roentgenium has a large energy difference between the bcc and fcc structure, amounting to $E_{bcc} - E_{fcc} = -21$ mRy. However, it should be noted that also the lighter homologue of roentgenium, namely silver, is barely stable in the fcc

structure, having the calculated energy difference $E_{bcc} - E_{fcc} = +2$ mRy. The same is true for the other group 11 elements copper and gold as well [23].

To find an explanation for this anomalous behaviour we begin by plotting the ℓ-resolved density of states (DOS) for roentgenium in the bcc structure using both the SR (dashed line) an NR (full line) approximations, see lower figure 3.4. As SR terms are taken into account, the bands broaden by a large amount. This effect is not as strong in silver, see upper figure 3.4. For the d-states of roentgenium, this band broadening is so large that the d-band crosses the Fermi level, while the lower band edge is relatively unchanged. In the NR limit, we get that $E_{bcc} - E_{fcc} = +1$ mRy for roentgenium, which favours the fcc structure. This indicates that the SR terms are important in the determination of the structural configuration.

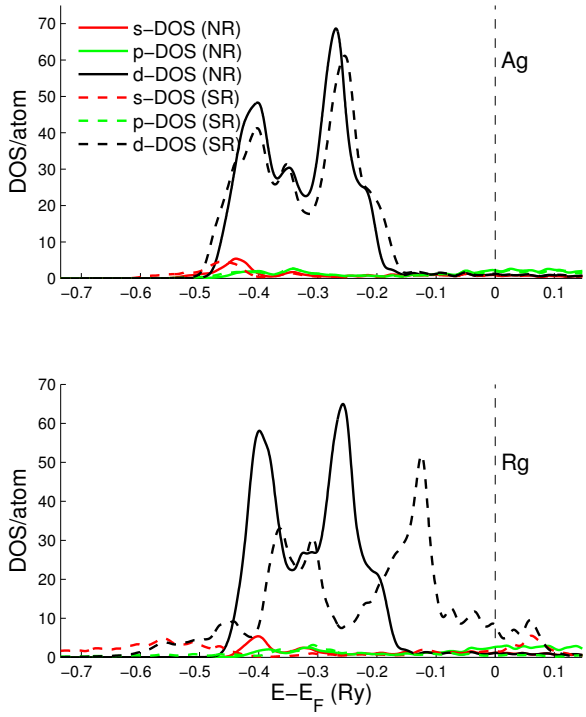

Figure 3.4. ℓ-resolved density of states for the $4d$-metal silver (Ag) and the $6d$-metal roentgenium (Rg) in the bcc structure, using nonrelativistic and scalar relativistic approximations. Note the large band broadening for roentgenium when scalar relativistic terms are taken into account.

The physics behind the band broadening can be viewed in two steps [33]. First, the relativistic effects lead to a shrinking s- and p-shell radii, which lead to a more effective screening of the nucleus than in the nonrelativistic case [34]. Due to this improved screening, the d-states feel a reduced attraction to the nucleus, and are more delocalised

in space. This will push the upper d-band edge to higher energies, shifting the band upwards. Secondly, as the d-states are now more extended they have greater overlap, which broadens the DOS. For the group 11 metals this results in a relatively unchanged lower band edge.

The large change in the DOS for roentgenium makes it possible to explain why it favours the bcc phase over the fcc one, as we will now argue. First we would like to point out the work by Singh [35], where it was shown why mercury (Hg) favours the fcc structure over the hcp structure. There it was argued that the relativistic lowering of the s-potential will lead to an increased hybridization between s- and p-states. It was then argued that charge transfer from $s \to p$ will lead to a favouring of the fcc structure.

Our argument is similar. In the case of roentgenium we also have a s-potential lowering (as can be seen by observing the s-DOS in figure 3.4) when SR terms are added. However, in this case we have a larger hybridization with the d-states, since the d-states are now delocalised as explained earlier. This leads to a transfer of charge from the d-states to the s-states when going from NR to SR approximations. This is seen in table 3.3 where the number of states at the Fermi level is tabulated for roentgenium in fcc and bcc structures, using different relativistic approximations. Since the s-states have a larger spatial extension, it is reasonable to assume that a charge transfer $d \to s$ leads to a larger interstitial charge density. An indication of the magnitude of charge in the interstitial can be obtained by looking at the first non-zero multipole moment Q_{40} of the charge density, where the multipole moment is defined as

$$Q_{\ell m} = \frac{\sqrt{4\pi}}{2\ell+1} \int \left(\frac{r}{w}\right)^{\ell} n(\mathbf{r}) Y_{\ell m}(\theta, \phi) \mathrm{d}\mathbf{r} - Z\delta_{0,0}. \tag{3.5}$$

Here the integration is performed over the Wigner-Seitz cell, and $Y_{\ell m}$ is the real harmonics while Z is the nuclear charge. Q_{40} is tabulated in table 3.3, where it is seen to increase as SR terms are taken into account.

Table 3.3. Number of d- and s-states at the Fermi level and first non-zero multipole moment Q_{40}.

NR	d	s	Q_{40}	SR	d	s	Q_{40}
fcc Rg	9.656	0.689	0.028	fcc Rg	9.060	1.223	0.029
bcc Rg	9.650	0.693	0.030	bcc Rg	8.967	1.300	0.034
fcc Ds	8.794	0.584	0.033	fcc Ds	8.030	1.085	0.040
bcc Ds	8.807	0.583	0.036	bcc Ds	8.014	1.147	0.046

Since a large charge density in the interstitial will lead to stronger electrostatic interactions between the ions, it is reasonable to assume that this will favour a bcc crystal structure. This is because the bcc structure is the most stable configuration if only electrostatics are taken into account, see section 3.2.1 for an explanation. In the case of

darmstadtium the d-states cross the Fermi level both in the NR and SR approximations (see figure 4 in Paper I), as is also the case for the other group 10 elements. The same mechanism of $d \rightarrow s$ charge transfer as for roentgenium applies, as is seen in table 3.3, and the bcc-fcc energy difference equals $E_{bcc} - E_{fcc} = +1$ mRy in the NR limit, making fcc the most stable structure.

To conclude this chapter, we note that the $6d$-metals behave in much the same way as their lighter homologues in the periodic table. However, for the noble metals anomalous behaviour surface, which can be explained by considering how the charge density is modified when relativistic effects are introduced.

Chapter 4

Analytic continuation

In this chapter we investigate the analytic continuation needed for the many-body implementation outlined in section 2.2.1, namely the Padé approximant, which is introduced in section 4.1. In section 4.2.1 we discuss some of the problems and issues which surface when one implements the Padé approximant in electronic structure theory, and discuss possible solutions. Section 4.2.2 discusses earlier studies of the Padé approximant, and in section 4.2.3 we investigate new methods.

4.1 Padé approximants - definition

We begin by defining the function $\tilde{f}(z)$, a rational complex function of the form

$$\tilde{f}(z) := \frac{\sum_{i=1}^{n+1} a_i z^{i-1}}{\sum_{i=1}^{m+1} b_i z^{i-1}} = \frac{a_1 + a_2 z + a_3 z^2 + \cdots + a_{n+1} z^n}{b_1 + b_2 z + b_3 z^2 + \cdots + z^m}, \tag{4.1}$$

i.e. a quotient of two polynomials. Notice that $b_{m+1} := 1$. The nominator polynomial will be of maximum order n, $n \geqslant 0$, and the denominator polynomial of maximum order m, $m \geqslant 0$. The polynomial coefficients are in general allowed to be complex, $(a_i, b_i) \in \mathbb{C}$. Now, we can define the type-I *Padé approximant* [36, 37] of order $[n/m]$ of a function $f(z)$ as the function of the form $\tilde{f}(z)$ which agrees with $f(z)$ up to the highest possible order. Assuming that the function f has a power series expansion $f(z) = \sum_{i=1}^{\infty} c_i z^{i-1}$, this condition implies that the coefficients in (4.1) should satisfy

$$\sum_{i=1}^{\infty} c_i z^{i-1} - \frac{\sum_{i=1}^{n+1} a_i z^{i-1}}{\sum_{i=1}^{m+1} b_i z^{i-1}} = c_{n+m+2} z^{n+m+1} + c_{n+m+3} z^{n+m+2} + \cdots \tag{4.2}$$

The problem of finding the polynomial coefficients when given the Taylor coefficients $c_i = \frac{f^{(i-1)}(0)}{(i-1)!}$ is then formulated as a linear system of equations. It can be noted that Padé

approximants should in general give better approximations than Taylor expansions to functions that contain simple poles. This is because they are rational polynomial functions, and hence contain poles by default.

If the value of a function $f(z)$ is given for a discrete set of N complex points $z_1, z_2, ..., z_N$ one can construct a so-called N-point (or type-II) Padé approximant. The condition is then that the following relation should hold:

$$\begin{aligned} f(z_1) &= \tilde{f}(z_1) \\ f(z_2) &= \tilde{f}(z_2) \\ f(z_3) &= \tilde{f}(z_3) \\ &\vdots \\ f(z_N) &= \tilde{f}(z_N). \end{aligned} \tag{4.3}$$

This is exactly the problem that we have when we perform the analytic continuation outlined in section 2.2.1. There, we have a Green's function $G(z_i)$ calculated for a set of complex energies z_i along a contour in the complex energy plane. This function has to be known on the Matsubara frequencies $i\omega_j$ along the imaginary axis. To perform this analytic continuation, we use the values of the Green's function known for the complex energies z_i and construct an approximant of the form (4.1), demanding that the relations in (4.3) should hold. Once we know $G(i\omega_j)$ for the Matsubara frequencies the many-body solver can be called. After the many-body problem is solved we have a self-energy $\Sigma(i\omega_j)$ known for the Matsubara frequencies, that we now need to know for the energy points z_i along the complex contour. Hence we now construct an approximant for the self-energy, using the same procedure as for the Green's function. It is hence this type-II Padé approximant that will be our main interest, and we will refer to it simply as a Padé approximant of order N from now on. In the next two sections we will review two methods that can be used to construct this Padé approximant.

In this thesis the functions to be approximated have the asymptotic behaviour $f(z) \to 1/|z|$ as $|z| \to \infty$. Hence the approximants should be of the order $n = m - 1$, i.e. the denominator polynomial should be one order higher than the nominator polynomial. To see this, consider a Green's function $G(z)$ in an electronic structure calculation. As implied in section 2.2, it will have simple poles at the eigenvalues of its corresponding Hamiltonian. Using partial fraction decomposition the Green's function can be written as a sum running over the eigenvalues E_i, viz.

$$G(z) = \sum_i \frac{w_i}{z - E_i}, \tag{4.4}$$

where w_i is the residue (or *weight*) of the i'th pole. Summing this together will give a rational polynomial function where the denominator polynomial has a order one larger than the nominator order.

Later in this thesis it will be important to know the poles and zeros of the approximant, i.e. the, in general complex, roots of the denominator and nominator polynomials respectively. These are found using a root-search algorithm [38, 39] for each of the two polynomials separately, and we will denote the zeros of the approximant as p_i and the poles as q_i.

4.1.1 Matrix formulation

Perhaps the most transparent way to construct a Padé approximant is by formulating it as a matrix equation, as was done by Beach et al. [40]. Assume that we are given a set of N function values $f(z_1), f(z_2), \cdots, f(z_N)$ for N number of (complex) points $z_1, z_2, \cdots, z_N$. The goal is to construct a $[\frac{N}{2} - 1/\frac{N}{2}]$ approximant. Setting $M := N/2$, the following system of equations should be solved:

$$\begin{aligned}
\frac{a_1 + a_2 z_1 + \cdots + a_M z_1^{M-1}}{b_1 + b_2 z_1 + \cdots + b_M z_1^{M-1} + z_1^M} &= f(z_1) \\
\frac{a_1 + a_1 z_2 + \cdots + a_M z_2^{M-1}}{b_1 + b_2 z_2 + \cdots + b_M z_2^{M-1} + z_2^M} &= f(z_2) \\
&\vdots \\
\frac{a_1 + a_2 z_N + \cdots + a_M z_N^{M-1}}{b_1 + b_2 z_N + \cdots + b_M z_N^{M-1} + z_N^M} &= f(z_N).
\end{aligned}$$

If each of the N equations are multiplied by their respective denominators, the terms can be rearranged to give the matrix equation $Av = b$, where

$$A = \begin{pmatrix}
1 & z_1 & \cdots & z_1^{M-1} & -f(z_1) & -f(z_1)z_1 & \cdots & -f(z_1)z_1^{M-1} \\
1 & z_2 & \cdots & z_2^{M-1} & -f(z_2) & -f(z_2)z_2 & \cdots & -f(z_2)z_2^{M-1} \\
\vdots & \vdots & \vdots & \vdots & \vdots & \vdots & \vdots & \vdots \\
1 & z_N & \cdots & z_N^{M-1} & -f(z_N) & -f(z_N)z_N & \cdots & -f(z_N)z_N^{M-1}
\end{pmatrix}$$

and

$$\begin{aligned}
v &= [a_1 \cdots a_M \; b_1 \cdots b_M]^T \\
b &= [z_1^M f(z_1) \cdots z_N^M f(z_N)]^T.
\end{aligned}$$

The unknown coefficient vector v can then be found by matrix inversion of A. Nothing can be said about the matrix A concerning sparsity and bandedness etc., hence the matrix inversion will be of $O(N^3)$ complexity. It should also be noted that A is an ill-conditioned matrix, making its inversion nontrivial. See Beach et al. [40] for details.

4.1.2 Thiele algorithm

The calculation of the approximant can be speeded up by the use of recursive methods. One such method is the Thiele reciprocal difference method [36, 37, 41], which constructs a continued fraction form of the Padé approximant:

$$\tilde{f}(z) = \cfrac{a_1}{1 + \cfrac{(z - z_1)a_2}{1 + \cfrac{(z - z_2)a_3}{\ddots\ 1 + \cfrac{(z - z_{i-1})a_i}{1 + (z - z_i)g_{i+1}(z)}}}}, \tag{4.5}$$

where the a_i's are the continued fraction coefficients that makes the approximant fit to the input data. The g_i's are defined as

$$g_1(z) = f(z),\ g_i(z) = \frac{g_{i-1}(z_{i-1}) - g_{i-1}(z)}{(z - z_{i-1})g_{i-1}(z)},\ i \geqslant 2. \tag{4.6}$$

The a_i's can be shown to be equal to $a_i = g_i(z_i)$ by the use of induction, viz.

$$\begin{aligned} g_i(z) = & \frac{a_i}{1 + (z - z_i)g_{i+1}(z)} = \\ & \frac{a_i}{1 + (z - z_i)\frac{g_i(z_i) - g_i(z)}{(z - z_i)g_i(z)}} = \\ & \frac{a_i}{\frac{g_i(z_i)}{g_i(z)}} \ \Leftrightarrow\ a_i = g_i(z_i), \end{aligned} \tag{4.7}$$

where (4.5) and (4.6) where used. Putting $z = z_1$ in Eq. (4.5) gives $\tilde{f}(z_1) = a_1$. Putting the rest of the points $z_2, z_3, ...$ in sequence one sees that Eq. (4.5) gives the correct fit. Using the a_i's the approximant can be evaluated at a point z using a recursive expression:

$$\begin{aligned} & \tilde{f}(z) = \frac{A_N}{B_N} = \frac{A_{N-1} + (z - z_{N-1})a_N A_{N-2}}{B_{N-1} + (z - z_{N-1})a_N B_{N-2}}, \\ & A_0 = 0,\ A_1 = a_1,\ B_0 = B_1 = 1. \end{aligned} \tag{4.8}$$

If the number of input points is N, N being odd, $\tilde{f}(z)$ will be a $[\frac{N-1}{2}/\frac{N-1}{2}]$ approximant. If N is even the approximant will be of order $[\frac{N}{2} - 1/\frac{N}{2}]$. The computation will be of $O(N^2)$ complexity.

4.2 Analytic continuation in electronic structure theory

4.2.1 Possible issues concerning the approximant

Analytic continuation is a so-called *ill-posed* problem in numerical analysis, meaning that its solution is very sensitive to small changes of the input values. We stress that this

is not a feature specific to the Padé approximant, but rather to the problem of numeric analytic continuation in general. However, if high enough precision is used during computations, very accurate solutions can still be found, as was shown for the Padé approximant in Ref. [40]. Electronic structure codes are usually written in low-level languages like FORTRAN or C/C++, where high precision is usually not available. However, reasonable good accuracy can still be reached, as we wish to show in this thesis.

Another issue is how to choose the order of the approximant. As is apparent from sections 4.1.1 and 4.1.2, if one would like to approximate a function having M poles, one should use twice as many input points $N = 2M$. However, usually one has no *a priori* knowledge of how many poles the function has. If too few input points are used, the approximant will obviously have difficulties in capturing the correct structure of the function. If too many input points are used, there will be more poles in the approximant than in the true function. Looking at the formulation in section 4.1.1, the system of linear equations will be over-complete. If arbitrary precision is used, the approximant will cancel a spurious pole by placing a zero of the nominator at the same location as the pole. However, if the precision is not good enough, or if the input data is contaminated by errors, this cancellation will not be perfect. These spurious pole-zero pairs are defects in the approximant. As will be seen, these defects can affect the electronic structure calculations. In principle, the defects could be removed manually from the approximant by the operation

$$\tilde{f}(z) \to \tilde{f}(z) \prod_i \frac{z - q_i}{z - p_i}, \tag{4.9}$$

where the product should run over all spurious poles and zeros.

To see how these defects can have an effect on calculations, we consider a test case of solid hydrogen. First, fcc hydrogen is self-consistently run to convergence using the EMTO method. After convergence the Green's function is explicitly calculated for the first few Matsubara frequencies. We use these function values as input to construct a Padé approximant, and this approximant is used to calculate the density of states along a horizontal contour close to the real axis. This approximant is then compared with the exactly calculated density of states. The test case has a setup similar to that used in Paper II, please see section V in Paper II for further details. This procedure of analytic continuation is not the same as for those used in the EMTO+DMFT method, but it is however a critical test of the approximant since it evaluates its ability to capture the fine structure of the density of states.

In figure 4.1 (left) the density of states constructed using a $N = 42$ Padé approximant is compared with the true function. Also plotted in figure 4.1 (right) is the approximant pole-zero distribution in the complex plane. Note that the approximant has an unphysical peak situated about 0.5 Ry below the Fermi level. By studying the pole-zero distribution one sees that a pole-zero pair situated at about 0.5 Ry below the Fermi level, close to the real axis, is the cause for this unphysical peak. By explicitly removing this pole-zero pair the peak disappears. As seen, these defects can indeed effect computa-

tions done using the Padé approximant.

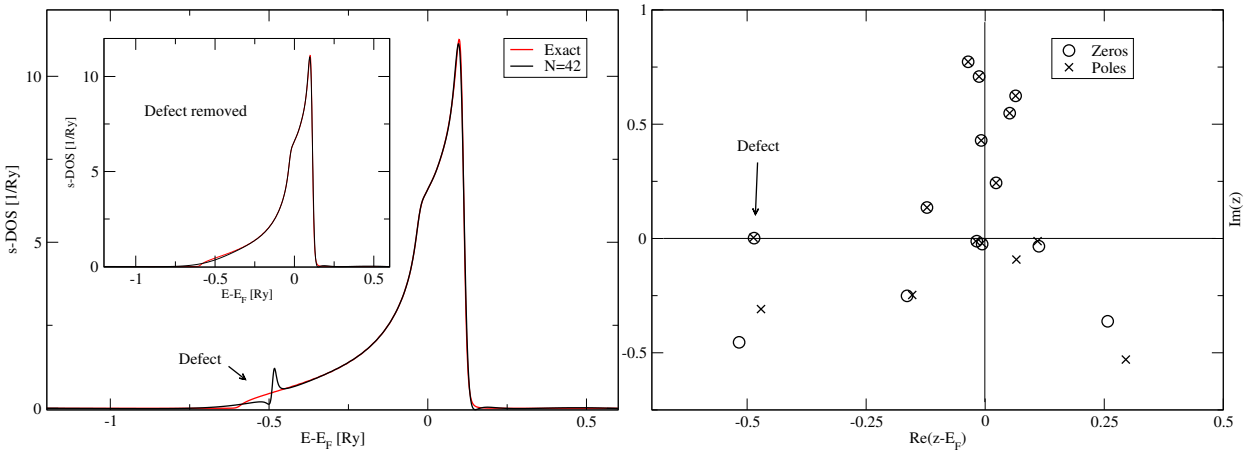

Figure 4.1. Left: Density of states of solid hydrogen constructed using a $N = 42$ Padé approximant, using input data from the Matsubara frequencies. Exact density of states plotted for comparison. Note the unphysical peak close to the bottom of the band, due to a defect in the approximant. Inset: Same as main figure, but with the defect removed explicitly. Right: Pole-zero distribution of the approximant. Six poles and six zeros farther out in the complex plane not shown. Note the defect pointed out by the arrow.

A pertinent question is how one is to decide which poles are physical and which are spurious. The most obvious way would be to make a geometric search in the complex plane and investigate whether a chosen pole has a zero in its neighbourhood. One of the simplest ways would be to let the neighbourhood be a circle of some predefined radius. However, this straightforward method has some pitfalls. It is for example not obvious how to specify the neighbourhood in the most optimal way since the pole-zero pairs usually have different separations. If the neighbourhood is defined too large, then more than one zero can be present inside, leading to ambiguity or the accidental removal of a physical zero. If on the other hand the neighbourhood is chosen too small, a spurious pole in a pole-zero pair with a large separation could mistakenly be considered as a true pole of the approximant. Hence, in practice, this method is difficult to implement inside any self-consistent loop, where an algorithm would be necessary to automate the filtering of defects. A schematic picture illustrating the geometric search is shown in figure 4.2.

Another issue which presents itself is which kind of Green's function that one should analytically continue. In the present implementation it is the **k**-integrated Green's function $G(z) = \int_{BZ} G_{RLR'L'}(\mathbf{k}, z) d\mathbf{k}$ which is analytically continued to the imaginary axis, as discussed in section 2.2.1. Numerically, this function is a sum over **k**-points in the irreducible Brillouin zone of the **k**-resolved Green's function $G(\mathbf{k}, z)$. The **k**-integrated Green's function is hence a sum of several (as many as there are **k**-points) functions, each of which contains one or several poles. If one instead would perform the analytic

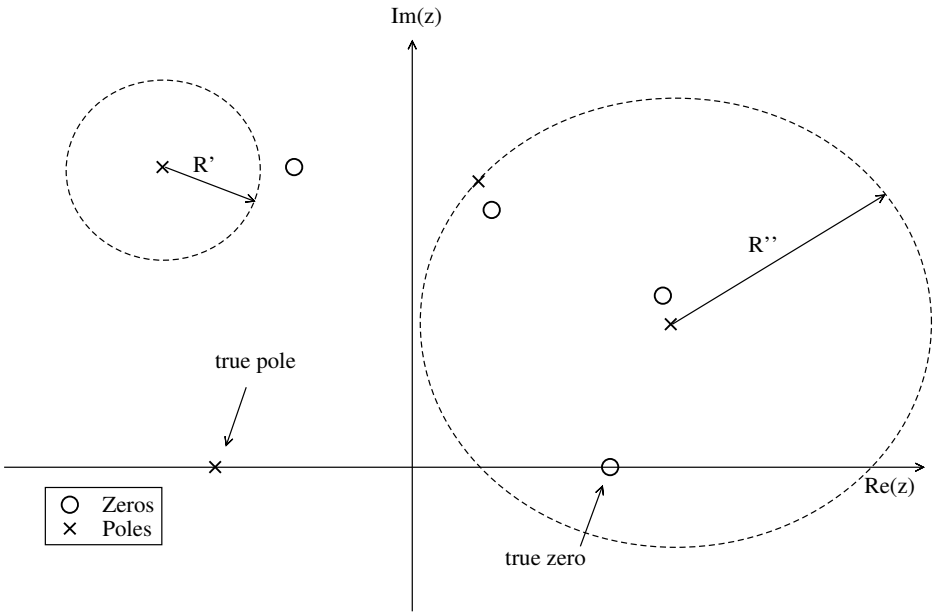

Figure 4.2. Schematic figure of a hypothetical geometric pole-zero search in the complex plane. The picture shows a true pole and a true zero of the approximant, located along the real axis. The rest of the poles and zeros are defects. To the left a too small neighbourhood (a circle with radius R') is chosen, not detecting the zero in the pole-zero pair. In the right part of the figure the neighbourhood (circle with radius R'') is too large. This circle not only includes the zero belonging to the pole-zero pair, but also the zero coming from another pair as well as a true zero of the approximant.

continuation for each of the **k**-resolved Green's functions, one would construct the Padé approximant for several simpler functions. The Bloch sum could then be performed *after* the analytic continuation is done. A schematic picture of this procedure is seen in figure 4.3.

4.2.2 Previous studies

The first use of Padé approximants for analytic continuation was by Vidberg and Serene [41] who used the Thiele algorithm to analytically continue spectral functions from the Matsubara frequencies to the real axis. They noticed the ill-posedness of the problem and the need for high accuracy, as well as the introduction of defective pole-zero pairs, having similar distributions as what was found in figure 4.1. In that work it was also concluded that an approximant could be considered good if the number of poles in the lower half-plane remained constant on the inclusion of further input points.

Later, Beach et al. [40] made further investigations of the Padé approximant by using the matrix formulation. They showed that the analytic continuation of spectral functions

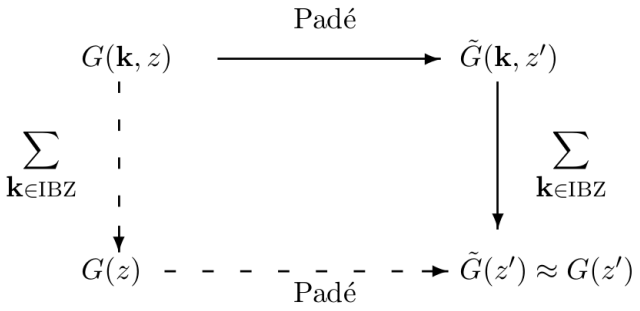

Figure 4.3. Schematic diagram of the analytic continuation before (straight path) or after (dashed path) Bloch summation. $G(\mathbf{k}, z)$ in the top left corner is given for a set of points. The goal is to obtain an analytic expression $\tilde{G}(z')$ (lower right corner) that can be used to approximate the true function $G(z')$. Following the straight path, the Padé approximant needs to be constructed for each $\mathbf{k} \in$ IBZ and the Bloch sum is performed at the desired point. Along the dashed path, only one single Padé approximant is needed.

could be performed with high accuracy by using symbolic software, enabling arbitrary precision calculations. Further, a goodness-of-fit test was constructed by investigating the polynomial coefficients.

The Padé approximant has also been used in the field of scattering theory by Sokolovski et al. [38]. The functions that were approximated were of a different kind (S-matrix elements) than the Green's functions presented in this thesis, but spurious poles and zeros occurred there as well. One observation done in that study was that the placement of these defects where sensitive to the addition of random numbers to the input data, while the placement of the true poles were more stable. Hence random numbers could be used to separate true and spurious poles in the approximant.

4.2.3 New developments and results

In this section we investigate the issues presented in section 4.2.1 and possible solutions to them. As a test case we use solid hydrogen in the fcc structure, without adding many-body effects. The Green's function is calculated for the Matsubara frequencies (temperature $T = 500$ K) and then analytically continued to a horizontal complex contour on which the density of states is calculated. Comparison is then made with the exactly calculated density of states, and the following error measure is introduced, viz.

$$Error(E) = |DOS(E) - DOS_{app}(E)|, \tag{4.10}$$

where $DOS_{app}(E)$ is the approximated density of states as a function of energy. This is done for several different approximant orders for the **k**-integrated and **k**-resolved

Green's function, and the result is seen in figure 4.4. As seen the **k**-integrated approximant gives a somewhat good fit of the true function, and is able to capture the band width. However, it fails to capture the density of states faithfully at the band edges, where it over- or undershoots the true value. The **k**-resolved approximant does in general give a better fit than does the **k**-integrated approximant. The price that has been paid is that more approximants (the same amount as the number of **k**-points) has to be constructed in this former case. However, the order (i.e. the number of input points N) can be made lower for each of these **k**-resolved approximants.

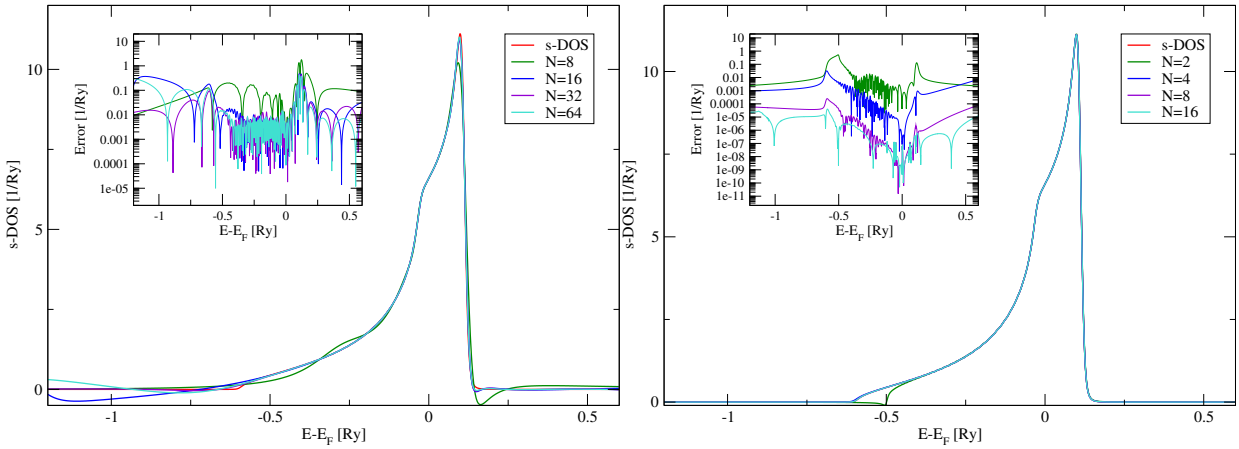

Figure 4.4. Left: **k**-integrated approximants for the density of states compared with exact value. The number of input points are $N = 8, 16, 32$ and 64. Right: **k**-resolved approximants for the density of states compared with exact value. The number of input points are $N = 2, 4, 8$ and 16.

There still remains the problem of how to deal with the spurious poles and zeros of the approximant. As was discussed in section 4.2.2, Sokolovski et al. [38] used randomly generated numbers to separate the defects from the true poles. We will proceed in a similar manner by introducing random factors of the form:

$$1 - \eta x_i, \quad i = 1, ..., N, \tag{4.11}$$

where η is a real scaling factor and the x_i's are real random numbers between -0.5 and 0.5, i.e. a random number close to 1, depending on the magnitude of η. These random numbers are multiplied with the input Green's functions, and the new pole-zero distribution is compared with the original distribution (where $\eta = 0$). This is done for the Γ-point of the $N = 16$ **k**-resolved approximant (see right figure 4.4), and the resulting pole-zero distributions can be seen in figure 4.5, for two different values of η. The black symbols correspond to $\eta = 0$, while red correspond to $\eta \neq 0$. The Γ-point has a physical pole situated about 0.6 Ry below the Fermi level, and this pole is relatively stable compared to the defective poles for $\eta = 10^{-6}$ (left figure). For $\eta = 10^{-3}$ the physical pole also shows a larger scattering, hence the magnitude of the random numbers needs to be chosen with care.

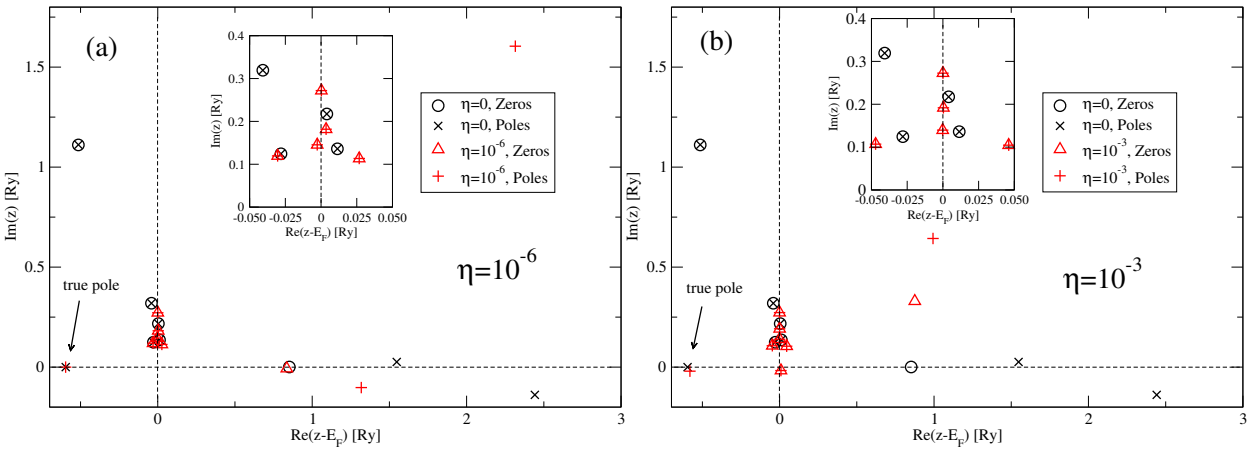

Figure 4.5. Left: Pole-zero distribution for $\eta = 0$ and $eta = 10^{-6}$. Right: Same as left, but here $\eta = 10^{-3}$.

More information can be extracted about the poles of the approximant by investigating their residues w_i. These are shown in table 4.1 for the $N = 16$ approximant of the Γ-point. The true pole is marked by a star in the table, and it has a residue close to one, with a small imaginary part. The other poles all have residues with small magnitudes, negative values or large imaginary parts, which indicates that they are unphysical.

Table 4.1. Real and imaginary parts of the $N = 16$ approximant poles with respective residues. The pole $i = 5$ ($\star$) is a true pole of the approximant, while the rest (†) are spurious. The poles can be seen plotted (black, $\eta = 0$) in figure 4.5.

i	$Re(q_i)$	$Im(q_i)$	$Re(w_i)$	$Im(w_i)$
† 1	$1.1449469 \cdot 10^{-2}$	0.1360169	$-2.6324331 \cdot 10^{-13}$	$-4.5109522 \cdot 10^{-13}$
† 2	$-4.0764097 \cdot 10^{-2}$	0.3192908	$-1.3977842 \cdot 10^{-10}$	$6.7675740 \cdot 10^{-11}$
† 3	-0.5137978	1.111784	$1.0184415 \cdot 10^{-3}$	$-1.3286583 \cdot 10^{-4}$
† 4	$4.0205983 \cdot 10^{-3}$	0.2173124	$-1.2889500 \cdot 10^{-13}$	$-2.2621590 \cdot 10^{-13}$
$\star$ 5	-0.5958811	$-3.5719320 \cdot 10^{-6}$	0.9999138	$4.7717123 \cdot 10^{-5}$
† 6	$-2.8055273 \cdot 10^{-2}$	0.1243891	$1.6093394 \cdot 10^{-12}$	$-6.1991449 \cdot 10^{-13}$
† 7	1.547490	$2.5824822 \cdot 10^{-2}$	0.9696459	0.1238033
† 8	2.441888	-0.1386907	-1.142889	-0.1035025

When the true poles have been singled out, the approximant can be constructed by the

sum

$$\tilde{f}(z) = \sum_i \frac{w_i}{z - q_i}, \tag{4.12}$$

where the sum should be over physical poles only.

Here we end with a list of conclusions:

- Numerical analytic continuation is ill-posed, making it sensitive even to small errors. This can in principle be remedied by computing in high precision, but this is far from possible in many cases of interest.
- If high accuracy is needed, it is better to use the **k**-resolved approximant instead of the **k**-integrated one. The reason is that the analytic continuation is performed for a simpler function. The price that has to be paid is that several approximants has to be constructed in this case.
- Due to numerical errors and lack of precision, defects might enter into the approximant. These defects can be found by root-searching, after which they can be removed. To select out the true poles the use of random numbers and pole residues can be used.

Chapter 5

Concluding remarks and Future work

We have performed first principles calculations on the solid state of the $6d$ transition metals and found that they share many common properties with the lighter d-metals. We proposed that the discrepancies found in the $6d$-series can be attributed to relativistic effects, which cause changes in the charge density. Due to the nuclear instability of these elements, the experimental verifications of these findings seem far away at the time of writing. However, the synthesizing of heavier elements is a thriving field of research, and one does not know what the future has in store.

We have also considered implementational aspects of many-body effects in first principles calculations, where the analytic continuation of numerical data is an important task. Even though this problem is ill-posed, and need better precision than what is usually available in electronic structure calculations, the results presented in this thesis show that much information can still be gained about the involved functions.

In the future, the goal is to find the most optimal way to implement DMFT into the EMTO method charge self-consistently, using a numerically controlled analytic continuation. To this end, the Padé approximant should be continually investigated, as should other possible techniques. Another interesting research path which could be taken is to investigate the analytic continuation of functions containing branch cuts, which is not considered in this thesis. Once a new EMTO+DMFT method is available, methods from random alloy theory, like the coherent potential approximation (CPA), can be implemented as well. This would make it possible to calculate the properties of a host of new materials, while taking many-body effects into account.

Returning to the transition metals, recently large interest has been shown for heavy transition metal compounds where strong correlations play an important role, like for the iridates [42, 43]. Here relativistic effects and electron interactions intermingle to produce novel phenomena. Investigations of these elements using first principle methods combined with many-body techniques could be a fruitful endeavour.

Appendix A

Electrostatic lattice energy

Assuming periodic boundary conditions for the box of length L, the Fourier transform of the $V(r) = 1/r$-potential to $\mathbf{q}$-space can be defined as

$$V(r) = \frac{1}{L^3} \sum_{\mathbf{q}} V(q) e^{i\mathbf{q}\cdot\mathbf{r}}, \tag{A.1}$$

where

$$V(q) = \int d\mathbf{r} V(r) e^{-i\mathbf{q}\cdot\mathbf{r}}. \tag{A.2}$$

$V(q)$ can be shown to equal $V(q) = \frac{4\pi}{q^2}$ by making the replacement $V(r) \to \lim_{\lambda\to 0} V(r)e^{-\lambda r}$ in the integral in Eq. (A.2), which will make it convergent. The limit $\lambda \to 0$ will be taken only at the end of the following calculation:
The background-background energy in Eq. (3.2) can be written as

$$\begin{aligned}
&\frac{1}{2}\int\int d\mathbf{r}d\mathbf{r}' \frac{n^2}{|\mathbf{r}-\mathbf{r}'|} = \frac{n^2}{2L^3}\sum_{\mathbf{q}}\int\int d\mathbf{r}d\mathbf{r}' V(q) e^{-i\mathbf{q}\cdot\mathbf{r}'} e^{i\mathbf{q}\cdot\mathbf{r}} = \\
&\frac{n^2}{2L^3}\sum_{\mathbf{q}} L^3\delta(\mathbf{q}) \int d\mathbf{r}' V(q) e^{-i\mathbf{q}\cdot\mathbf{r}'} = \\
&\frac{n^2}{2} V(q=0) L^3,
\end{aligned} \tag{A.3}$$

where the definition of the delta function, $\delta(\mathbf{q}) = \frac{1}{L^3}\int d\mathbf{r} e^{i\mathbf{q}\cdot\mathbf{r}}$, was used. In the same way we get for the source-background part:

$$\begin{aligned}
&-\sum_i \int d\mathbf{r} \frac{n}{|\mathbf{r}-\mathbf{R}_i|} = -\frac{n}{L^3}\sum_i\sum_{\mathbf{q}}\int d\mathbf{r} e^{-i\mathbf{q}\cdot\mathbf{R}_i} V(q) e^{i\mathbf{q}\cdot\mathbf{r}} = \\
&-\frac{n}{L^3}\sum_i\sum_{\mathbf{q}} V(q) L^3\delta(\mathbf{q}) = \\
&-nV(q=0)N.
\end{aligned} \tag{A.4}$$

For the charge-charge interaction we use the lattice transform to get that

$$\frac{1}{2}\sum_{i\neq j}\frac{1}{|\mathbf{R}_i-\mathbf{R}_j|}=\frac{1}{2}\sum_{i\neq j}\int d\mathbf{r}\frac{\delta(\mathbf{r}-\mathbf{R}_j)}{|\mathbf{r}-\mathbf{R}_j|}=$$
$$\frac{1}{2L^3}\sum_{\mathbf{q}}\sum_{i\neq j}\int d\mathbf{r}V(q)e^{-i\mathbf{q}\cdot\mathbf{R}_j}e^{i\mathbf{q}\cdot\mathbf{r}}\delta(\mathbf{r}-\mathbf{R}_i)=$$
$$\frac{1}{2L^3}\sum_{\mathbf{q}}\sum_{i,j}\int d\mathbf{r}V(q)e^{-i\mathbf{q}\cdot\mathbf{R}_j}e^{i\mathbf{q}\cdot\mathbf{r}}\delta(\mathbf{r}-\mathbf{R}_i)-\frac{N}{2L^3}\sum_{\mathbf{q}}V(q)=$$
$$\frac{n}{2L^3}\sum_{\mathbf{q}}\sum_{j}\sum_{\mathbf{G}}\int d\mathbf{r}V(q)e^{-i\mathbf{q}\cdot\mathbf{R}_j}e^{i\mathbf{q}\cdot\mathbf{r}}e^{i\mathbf{G}\cdot\mathbf{r}}-\frac{N}{2L^3}\sum_{\mathbf{q}}V(q)=$$
$$\frac{n}{2L^3}\sum_{\mathbf{q}}\sum_{j}\sum_{\mathbf{G}}V(q)e^{-i\mathbf{q}\cdot\mathbf{R}_j}L^3\delta(\mathbf{G}+\mathbf{q})-\frac{N}{2L^3}\sum_{\mathbf{q}}V(q)=$$
$$nN\sum_{\mathbf{G}}V(G)-\frac{N}{2L^3}\sum_{\mathbf{q}}V(q), \tag{A.5}$$

where the expression for the charge in Eq. (3.3) was used, as well as the property $e^{i\mathbf{G}\cdot\mathbf{R}_i}=1$ of the reciprocal lattice vector. Adding together the singular terms ($G=q=0$) of Eqs. (A.3-A.5) will result in a term $-\frac{nV(0)}{L^3}$ that goes to zero in the thermodynamic limit $L\to\infty$. Only now can the limit $\lambda\to 0$ be taken, giving the electrostatic energy per particle U/N given in Eq. (3.4).

Acknowledgements

First and foremost I would like to thank my supervisor Prof. Levente Vitos for always being helpful and supporting during the work on this thesis. I would also like to express my gratitude to my co-supervisor Prof. Oscar Tjernberg for pointing me in the direction of the Applied Materials Physics group. The leader of the group, Prof. Börje Johansson, is also kindly thanked.

Part of the work behind this thesis was done while visiting the chair of Theoretical Physics III at the University of Augsburg. I would like to thank Prof. Liviu Chioncel for invaluable help in my work and for interesting discussions during my stays.
All the members of the chair of Theoretical Physics III are also acknowledged for their generous hospitality that made my visits pleasant.

A big thanks goes out to all former and present group members at the Applied Materials Physics group, no one mentioned, no one forgotten. Thanks to all of you the department is such a nice place to work at.

The Anders Henrik Göransson foundation and Bergshögskolans jubilary foundation are acknowledged for financial support. The National Supercomputer Centre in Linköping is acknowledged for computational resources.

Finally, I would also like to thank my family, who always supports me.

Bibliography

[1] P. Hohenberg and W. Kohn, Phys. Rev. **136**, B864 (1964).

[2] W. Kohn and L. J. Sham, Phys. Rev. **136**, A1133 (1965).

[3] R. M. Dreizler and E. K. U. Gross, *Density functional theory, an approach to the quantum many-body problem* (Springer Verlag, New York, 1990).

[4] A. Georges, G. Kotliar, W. Krauth, and M. J. Rozenberg, Rev. Mod. Phys. **68**, 13 (1996).

[5] G. Kotliar, S. Y. Savrasov, K. Haule, V. S. Oudovenko, O. Parcollet and C. A. Marianetti, Rev. Mod. Phys. **78**, 865 (2006).

[6] P. L. Taylor and O. Heinonen, *A quantum approach to condensed matter physics* (Cambridge University Press, Cambridge, 2002).

[7] J. Perdew and Y. Wang, Phys. Rev. B **45**, 13244 (1992).

[8] L. Vitos, *The EMTO Method and Applications*, Computational Quantum Mechanics for Materials Engineers (Springer-Verlag, London, 2007).

[9] O. K. Andersen, O. Jepsen, and G. Krier, *Lectures on Methods of Electronic Structure Calculation* (World Scientific, Singapore, 1994), p. 63.

[10] O. K. Andersen and T. Saha-Dasgupta, Phys. Rev. B **62**, R16219 (2000).

[11] L. Vitos, H. L. Skriver, B. Johansson and J. Kollár, Comp. Mat. Sci. **18**, 24 (2000).

[12] L. Vitos, Phys. Rev. B **64**, 014107 (2001).

[13] O. K. Andersen, C. Arcangeli, R. W. Tank, T. Saha-Dasgupta, G. Krier, O. Jepsen, and I. Dasgupta, *Tight-Binding Approach to Computational Materials Science*, edited by L. Colombo, A. Gonis, and P. Turchi, MRS Symposia Proceedings No. 91 (Materials Research Society, Pittsburgh, PA, 1998), p. 3-34.

[14] M. Zwierzycki and O. K. Andersen, Acta Phys. Pol. A **115**, 64 (2009).

[15] L. Chioncel, L. Vitos, I. A. Abrikosov, J. Kollár, M. I. Katsnelson and A. I. Lichtenstein, Phys. Rev. B **67**, 235106 (2003).

[16] M. I. Katsnelson and A. I. Lichtenstein, Eur. Phys. J. B **30**, 9 (2002).

[17] See F. Gross, *Relativistic quantum mechanics and field theory* (Wiley Science, 1999), for a review.

[18] L. V. Pourovskii, A. V. Ruban, L. Vitos, H. Ebert, B. Johansson and I. A. Abrikosov, Phys. Rev. B **71**, 094415(10) (2005).

[19] E. N. Economou, *The physics of solids, essentials and beyond* (Springer-Verlag, Berlin Heidelberg, 2010).

[20] D. A. Young, *Phase diagrams of the elements* (University of California Press, Berkeley, 1991).

[21] L. Fast, J. M. Wills, B. Johansson and O. Eriksson, Phys. Rev. B **51**, 17431 (1995).

[22] D. G. Pettifor, J. Phys. C **3**, 367 (1970).

[23] H. L. Skriver, Phys. Rev. B **31**, 1909 (1985).

[24] D. G. Pettifor, *Bonding and structure of molecules and solids* (Clarendon Press, Oxford, 1995).

[25] G. F. Giuliani and G. Vignale, *Quantum theory of the electron liquid*, sec. 1.6, (Cambridge University Press, Cambridge, 2005).

[26] Yu. Ts. Oganessian et al., Phys. Rev. Lett **104**, 142502 (2010).

[27] L. R. Morss, N. M. Edelstein, and J. Fuger, *The chemistry of the actinide and transactinide elements*, edited by L. R. Morss, N.M. Edelstein, and J. Fuger (Springer, Dordrecht, 2010), Vol. 3.

[28] N. Gaston, I. Opahle, H.W. Gäggeler, and P. Schwerdtfeger, Angew. Chem., Int. Ed. **46**, 1663 (2007).

[29] J. Noffsinger and M. L. Cohen, Phys. Rev. B **81**, 073110 (2010).

[30] A. Hermann, J. Furthmüller, H.W. Gäggeler, and P. Schwerdtfeger, Phys. Rev. B **82**, 155116 (2010).

[31] J. Gyanchandani and S. K. Sikka, Phys. Rev. B **83**, 172101 (2011).

[32] S. L. Shang et al. Comp. Mat. Sci. **48**, 813 (2010).

[33] H. Eschrig, M. Richter and I. Opahle, in: *Relativistic Electronic Structure Theory*, ed. P. Schwerdtfeger, Elsevier (2004).

[34] P. Pykkö, Chem. Rev. **88**, 563 (1988).

[35] P. P. Singh, Phys. Rev. Lett. **72**, 2446 (1994).

[36] G. A. Baker, *Essentials of Padé approximants* (Academic Press, New York, 1975).

[37] G. A. Baker and P. Graves-Morris, *Padé approximants* (Cambridge University Press, New York, 1984)

[38] D. Sokolovski, E. Akhmatskaya and S. K. Sen, Comp. Phys. Comm. **182**, 448 (2011).

[39] M. S. Petkovic, C. Carstensen and M. Trajkovic, Numer. Math. **69**, 353 (1995).

[40] K. S. D. Beach, R. J. Gooding and F. Marsiglio, Phys. Rev. B **61**, 5147 (2000).

[41] H. J. Vidberg and J. W. Serene, J. Low. Temp. Phys. **29**, 179 (1977).

[42] B. J. Kim et al., Phys. Rev. Lett. **101**, 076402 (2008).

[43] S. J. Moon et al., Phys. Rev. Lett. **101**, 226402 (2008).